In situ X-ray scattering study of the cubic to hexagonal transformation of AlN in $Ti_{1-x}Al_xN$

N. Norrby [a,*], L. Rogström [a], M.P. Johansson-Jõesaar [a,b], N. Schell [c], M. Odén [a]

[a] *Nanostructured Materials, Department of Physics, Chemistry and Biology (IFM), Linköping University, SE-581 83 Linköping, Sweden*
[b] *R&D Material and Technology Development, SECO Tools AB, SE-737 82 Fagersta, Sweden*
[c] *Helmholtz-Zentrum Geesthacht (HZG), Max-Planck-Str. 1, D-21502 Geesthacht, Germany*

Abstract

In the present work, we have studied the decomposition of arc-evaporated $Ti_{0.55}Al_{0.45}N$ and $Ti_{0.36}Al_{0.64}N$ during heat treatments in vacuum by in situ synchrotron wide-angle X-ray scattering primarily to characterize the kinetics of the phase transformation of AlN from the cubic (c) NaCl structure to the hexagonal (h) wurtzite structure. In addition, in situ small-angle X-ray scattering measurements were conducted to explore details of the wavelength evolution of the spinodal decomposition, thus providing information about the critical size of the c-AlN-rich domains prior to the onset of the transformation to h-AlN. We report the fractional cubic to hexagonal transformation of AlN in $Ti_{1-x}Al_xN$ as a function of time and extract activation energies between 320 and 350 kJ mol^{-1} depending on the alloy composition. The onset of the hexagonal transformation occurs ~50 K lower in $Ti_{0.36}Al_{0.64}N$ compared to $Ti_{0.55}Al_{0.45}N$ where the high Al content alloy also has a significantly higher transformation rate. A critical wavelength for the cubic domains of ~13 nm was observed for both alloys. Scanning transmission electron microscopy shows a c-TiN/h-AlN microstructure with a striking morphology resemblance to the c-TiN/c-AlN microstructure present prior to the hexagonal transformation.
© 2014 Acta Materialia Inc. Published by Elsevier Ltd. All rights reserved.

1. Introduction

As a protective hard coating on metal cutting inserts, $Ti_{1-x}Al_xN$ has been extensively studied over the years since its discovery in the 1980s [1,2] and has been shown to phase transform isostructurally via spinodal decomposition at elevated temperatures [3–7]. The spinodal decomposition, where the cubic (B1) solid solution of c-$Ti_{1-x}Al_xN$ decomposes into nanometer-sized coherent c-TiN- and c-AlN-rich domains [8–10], is responsible for a well-studied age hardening [11,12] at temperatures relevant for metal machining [13,14]. The age hardening has its main origin

in coherency strains and differences in elastic properties [15] between the c-TiN- and c-AlN-rich domains.

Subsequent to the spinodal decomposition, domain coarsening occurs [4,16,17] and the c-AlN-rich domains eventually transforms into the thermodynamically stable hexagonal (B4) phase, h-AlN. Initial small crystallites of h-AlN with a partial coherence with the cubic phases have been shown to improve the mechanical properties [18,19], while growth of the h-AlN crystallites results in the loss of this coherency. The poor mechanical properties of h-AlN together with the loss of coherency cause a marked reduction of the coating's hardness. It has previously been shown that the early stage of the cubic to hexagonal transformation is typically induced in c-AlN-rich domains close to grain boundaries with high diffusivity [9]. However,

* Corresponding author. Tel.: +46 13282907.
  E-mail address: nikno@ifm.liu.se (N. Norrby).

despite the adverse effect that formation of h-AlN has on the material performance, previous studies have almost exclusively focused on understanding the spinodal decomposition and how it can be influenced by, for example, alloying [20–25], pressure [26,27], multilayers [28,29] and metal cutting [30]. Wüstefeld et al. [31] used high-temperature glancing X-ray diffraction to study the effect of bias (–40, –80 and –120 V) on the spinodal decomposition and the c-AlN to h-AlN transformation at temperatures up to 850 °C and an increase in bias was shown to increase the fraction of h-AlN in the annealed coating. Mayrhofer et al. [32] studied the spinodal decomposition and hexagonal transformation kinetics with differential scanning calorimetry (DSC) at different heating rates for $Ti_{0.34}Al_{0.66}N$ and found slightly higher activation energy for the h-AlN transformation compared to the spinodal decomposition.

However, a detailed kinetic description of the transformation to the hexagonal structure at isothermal temperatures is lacking. In this paper, the evolution of h-AlN with time and temperature measured in situ by synchrotron wide-angle X-ray scattering (WAXS) for two different alloy compositions, $Ti_{0.55}Al_{0.45}N$ and $Ti_{0.36}Al_{0.64}N$, is reported. The measurements have been conducted on powders extracted from arc-evaporated coatings to enable a quantitative kinetic description of the transformation and growth of h-AlN. The results are presented as the phase fraction of h-AlN/c-AlN as a function of the isothermal time and the data is analyzed with a modified Kolmogorov–Johnson–Mehl–Avrami (KJMA) equation. Furthermore, in situ small-angle X-ray scattering (SAXS) is used to extract the domain size of c-AlN when it starts to transform to h-AlN. Complimentary transmission electron microscopy has been used to verify the in situ microstructural findings.

2. Experimental details

To generate the powder, $Ti_{1-x}Al_xN$ was grown on thin iron foils by cathodic arc evaporation in a Sulzer Metaplas MZR323 system. Depositions were performed in a 4.5 Pa N_2 atmosphere at an approximate substrate temperature of 500 °C and a substrate bias of either –40 or –20 V. Compound cathodes with a Ti/Al ratio of 33/67 and 50/50 were used. Prior to deposition, the iron foils were cleaned in an ultrasonic bath and etched with argon ions. After deposition, the iron foils were dissolved in hydrochloric acid, leaving flakes of the coatings, which were ground into a fine powder with a mortar and pestle in acetone. The Ti/Al ratio in the powder was measured by energy-dispersive X-ray spectroscopy in a Leo 1550 Gemini scanning electron microscope using a working distance of 8.5 mm and an acceleration voltage of 20 kV.

WAXS measurements were performed at PETRA III (beam line P07 DESY Photon Science) in Hamburg using an X-ray energy of 53.7 keV and a slit defined beam size of 500×500 μm^2, whereas SAXS measurements were accomplished using an X-ray energy of 73.9 keV and a beam size of 100×100 μm^2. The powder was put in a half

open cylinder with a radius of 750 μm as is shown schematically in Fig. 1.

The diffracted intensity in WAXS measurements was detected with 4 s exposures using a two-dimensional area detector (Perkin Elmer) with a resolution of 200 μm per pixel which was positioned 1330 mm from the sample. The exposure time for SAXS measurements was 80×0.1 s with a sample-to-detector distance of 3320 mm. The samples were inserted at a fixed position onto a loading bridge in a vacuum furnace operating at a pressure below 0.67 mPa at the maximum temperature (T_{max}). The heating was performed with a BN tube furnace connected to a Eurotherm controller with the thermocouple in close proximity to the sample. After heating the sample at a rate of 20 K min^{-1}, it was isothermally held at T_{max} for 4–6 h before a controlled cool-down of 20 K min^{-1} was performed. Prior to the annealing experiments, the temperature at the sample position was further calibrated by placing a polished Si wafer (with emissivity set to 0.22) at the sample position and measuring the temperature using a two-color CellaTemp pyrometer.

The sample-to-detector distance and the tilt of the detector were determined using a reference sample (Si powder for WAXS and LaB_6 powder for SAXS) and the software Fit2D [33]. After correcting for the geometrical set-up and transforming the two-dimensional exposures into one-dimensional lineouts, pseudo-Voigt functions were fitted to the WAXS diffraction peaks and the integrated intensities were extracted. Prior to SAXS analysis, an exposure without the sample present was subtracted to remove scattered intensity originating from the air and the furnace windows. The measured two-dimensional raw images were transformed into one-dimensional lineouts, plotting the intensity as a function of the reciprocal length (q). The software Igor Pro was used in combination with the
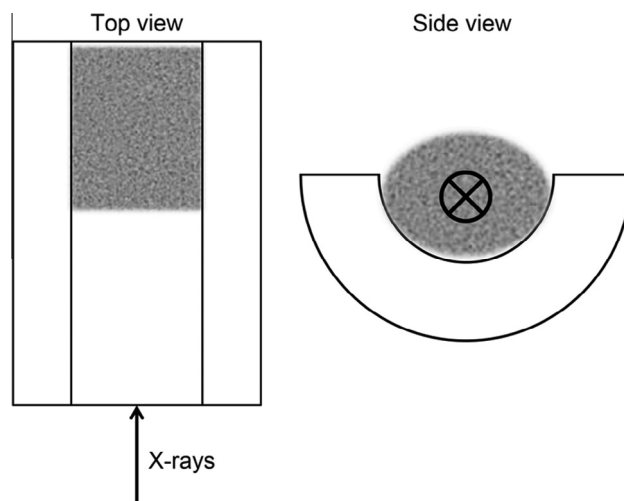

Fig. 1. A schematic view of the sample holder used for WAXS and SAXS measurements. The radius of the half circle is 750 μm with a beam size of 500×500 μm^2; the black crossed circle marks the beam position during measurements.

Unified fit in the Irena Package [34] to obtain the wavelength of the isostructurally decomposed domains.

Ex situ microstructural information was obtained on selected powders by scanning transmission electron microscopy (STEM) with a FEI Tecnai G^2 TF 20 UT analytical microscope operated at an acceleration voltage of 200 kV and a camera length of 220 mm. The powder was ground an additional time with a mortar and pestle to achieve electron transparency before placing it on a holey carbon grid.

3. Results and discussion

3.1. Analysis of raw data

Fig. 2 shows lineouts of $Ti_{0.36}Al_{0.64}N$ at different temperatures and isothermal times obtained after a rotational integration of the two-dimensional diffraction pattern from the detector. The spinodal decomposition is seen as a gradual broadening of the cubic $Ti_{0.36}Al_{0.64}N$ peaks which evolves into two separate c-AlN and c-TiN peaks. At the very early stage around 700 °C, the WAXS signal is not sufficient to distinguish the spinodal decomposition shown in the SAXS measurements in Fig. 11. At the onset of the transformation to h-AlN, the intensity of the c-AlN peak decreases with further growth of h-AlN.

The (1 0 0) h-AlN peak is magnified in Fig. 3a to illustrate the evolution of h-AlN. The first evidence of the hexagonal phase occurs at a temperature around 950 °C. From the lineouts it is also apparent that the increase in peak intensity is rapid at the beginning of the transformation and slows down with time; compare, for example, the difference between 50 and 150 min with the difference between 150 and 285 min. This is further shown in Fig. 3b where the integrated intensity of the h-100 peak at different annealing times is plotted for 950 and 1000 °C. A plateau in the integrated intensity is reached after around 120 min of isothermal annealing at 1000 °C
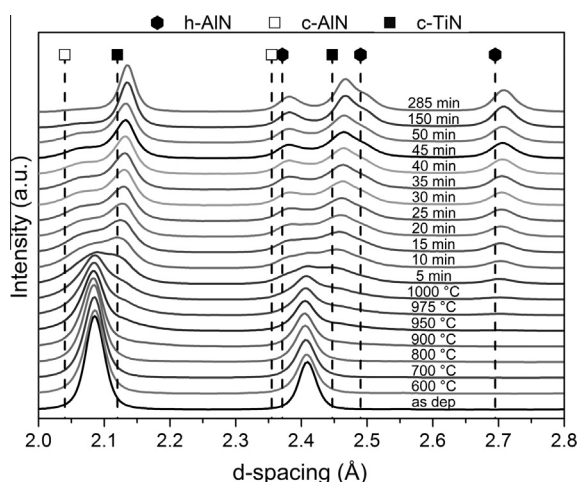

Fig. 2. Lineouts for $Ti_{0.36}Al_{0.64}N$ obtained at different temperatures during heating and at different isothermal temperatures. The markers for c-AlN, c-TiN and h-AlN are valid for room temperature.
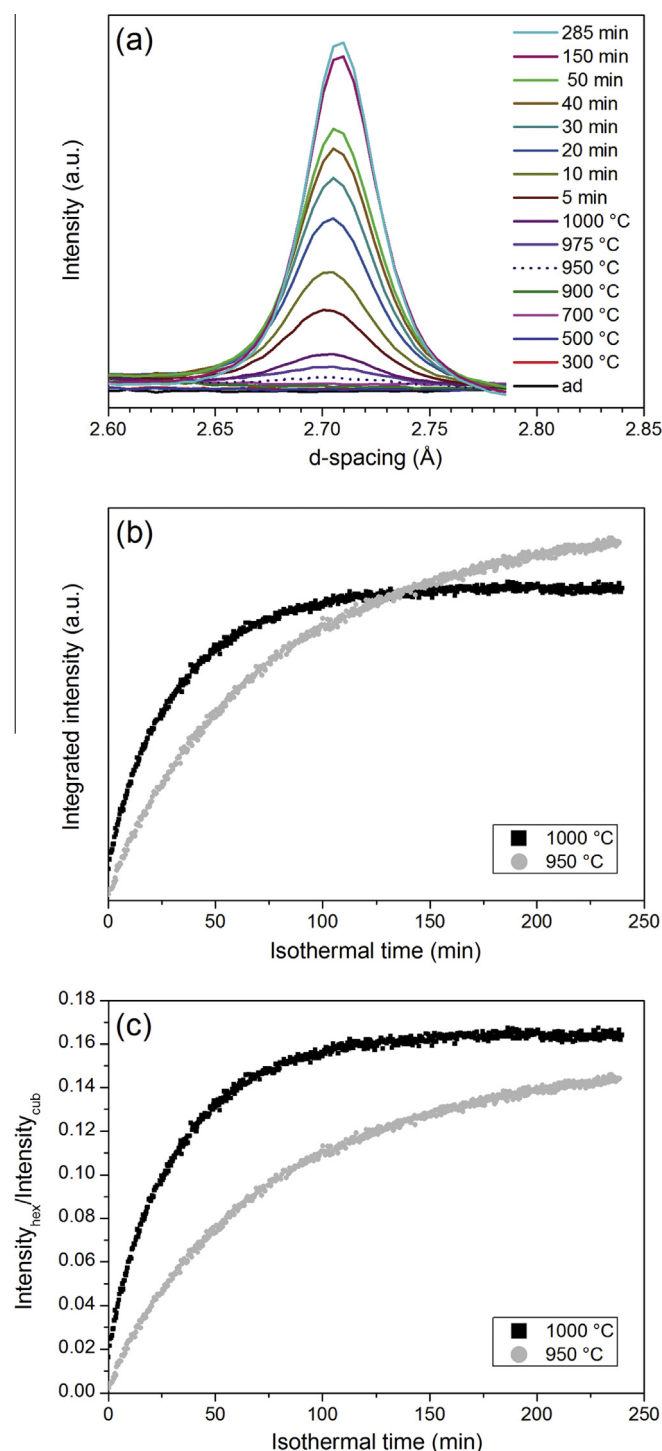

Fig. 3. The three first steps to transform the raw data into the h-AlN fraction formed, exemplified by results from $Ti_{0.36}Al_{0.64}N$, where (a) shows the integrated lineout from the raw data at different temperatures or isothermal times, (b) shows the integrated h-100 peak intensity as a function of isothermal time and (c) shows the data in (b) normalized with the averaged integrated intensity from the first 25 exposures of the cubic (2 0 0) c-TiAlN peak.

indicating a complete transformation of c-AlN to h-AlN, which is not seen when annealing at 950 °C. However, since the absolute intensity will depend on, for example, the illuminated sample volume, it will vary between different

measurements. This is exemplified in Fig. 3b where the absolute intensity is greater in the 950 °C sample despite an incomplete transformation and direct comparisons between the different measurements are hence not possible. Since this will also affect the absolute integrated intensity of the cubic peaks at the beginning of the annealing it is possible to obtain the fraction of c-AlN transformed into h-AlN by first dividing the absolute intensity of the h-AlN peak by the average integrated intensity from the 25 first exposures ($T < 500$ °C) of the cubic (2 0 0)-TiAlN. The result after such operation of the data in Fig. 3b is seen in Fig. 3c and the data after 950 and 1000 °C are now directly comparable with each other. The saturation value of 0.16 is related to the Al composition and the structure factors of c-TiAlN and h-AlN and is hence smaller for the low-Al-content powder.

From the assumption that the plateau seen in Fig. 3c represents a complete transformation of c-AlN to h-AlN, the fraction of h-AlN can be estimated by normalizing the data in Fig. 3c with the maximum value of the plateau. This assumption is supported by the fact that only traces of c-AlN could be detected in the WAXS patterns in the last exposures. The results presented in Fig. 4 show the fraction of h-AlN formed as a function of time for (a) $Ti_{0.36}Al_{0.64}N$ (Fig. 4a) and $Ti_{0.55}Al_{0.45}N$ (Fig. 4b). There is a significant difference in the h-AlN transformation rate between the two compositions. For example, after 120 min at 1000 °C, the transformation of $Ti_{0.36}Al_{0.64}N$ to h-AlN is completed while under the same conditions the h-AlN fraction in $Ti_{0.55}Al_{0.45}N$ is <0.4. In fact, to obtain a comparable transformation rate for $Ti_{0.55}Al_{0.45}N$ the temperature has to be raised to 1100 °C. The large difference in transformation rate with temperature indicates that the h-AlN transformation is governed by a thermally activated diffusion process via a nucleation and growth mechanism. Due to an unstable sample position during annealing, no data after around

30 min can be shown for $Ti_{0.36}Al_{0.64}N$ at 1050 °C, whereas the gap seen for $Ti_{0.55}Al_{0.45}N$ at 1100 °C is due to a temporary software problem during the exposures.

3.2. Kinetic analysis

The most frequently used method, e.g. for transformations in steels [35,36] and ceramic coatings [37], to extract kinetic information about phase transformations from experimental data is the KJMA equation [38–41]. The equation is presented in its differential form in Eq. (1) and after integration in Eq. (2):

$$df = (1 - f)dx \tag{1}$$

$$f = 1 - e^{-x}. \tag{2}$$

where f is the transformed fraction and x an Arrhenius expression, which for isothermal conditions is given by Eqs. (3) and (4):

$$x = (kt)^n \tag{3}$$

$$k = k_0 \exp\left(\frac{E_a}{RT}\right), \tag{4}$$

where t is the isothermal time, n is the Avrami constant, k_0 a pre-exponential constant, R the gas constant, T the absolute temperature and E_a the activation energy. For the KJMA equation to be valid a random homogenous nucleation in an infinitely large bulk where the nuclei grow without interfering with other nuclei is assumed. This is not fulfilled in the case of h-AlN growth as it has previously been reported to nucleate at grain boundaries [9,27,42]. Models that take grain boundary nucleation in account exist, and some of these are summarized and tested in simulations by Jägle and Mittemeijer [43]. One of these models modifies Eq. (1) with an impingement parameter, ε, which is shown in its differential state in Eq. (5) and in integrated form in Eq. (6).
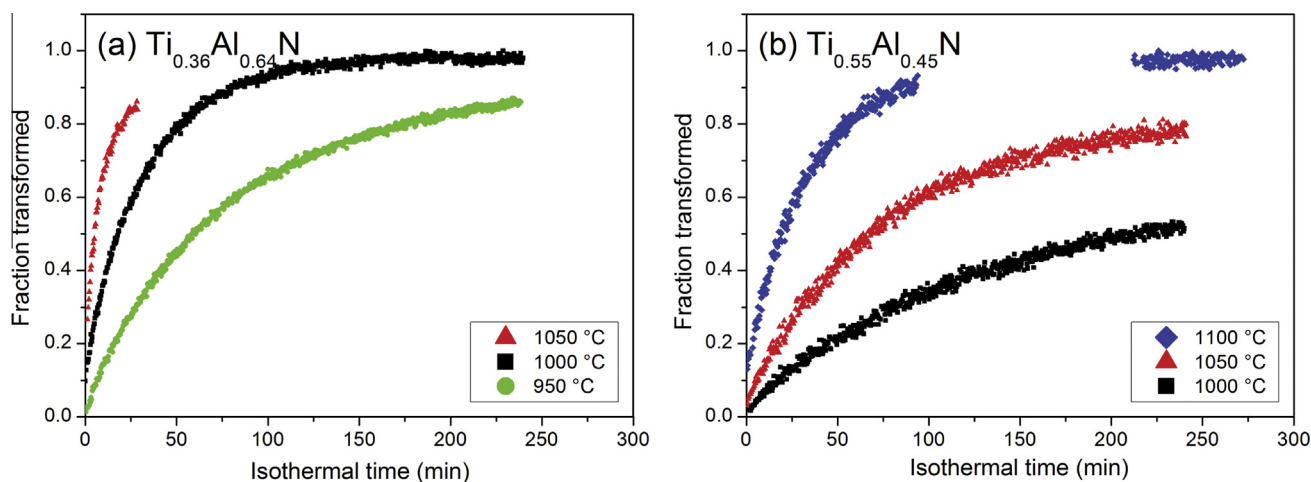

Fig. 4. The fraction of c-AlN transformed into h-AlN as a function of the isothermal time at three different temperatures for (a) $Ti_{0.36}Al_{0.64}N$ and (b) $Ti_{0.55}Al_{0.45}N$.

$$df = (1 - f)^{\varepsilon} dx \quad (5)$$

$$f = 1 - (1 + x(\varepsilon - 1))^{\frac{1}{1-\varepsilon}}. \quad (6)$$

According to Jägle et al., this model can well describe a system with a nucleation that does not deviate too strongly from random nucleation and has the advantage that the fitting procedure will be similar to the KJMA equation. Although a relation of the impingement parameter to any physical properties is lacking in the literature, values below unity are related to a weak impingement and values above unity are related to a strong impingement. Strong impingement typically occurs where the probability of nuclei interfering with each other increases, e.g. in grain boundaries. This leads to a slower transformation rate compared to Eq. (1) as interfering nuclei will hinder each other from growing further, similar to Ostwald ripening as described and illustrated by Molnar et al. [44]. However, if the nuclei are positioned far from each other with less risk of interfering, the impingement is weak with a faster transformation rate as compared to Eq. (1). This could also apply for h-AlN nucleation in $Ti_{1-x}Al_xN$ since the preceding spinodal decomposition leads to a periodic network of c-AlN-rich domains which when they nucleate into h-AlN have a much smaller probability of interfering with each other. To test the impingement present during the transformation in TiAlN, values of ε between 0.1 and 4 have been investigated. Eq. (6) can now be rewritten to form Eq. (7) (except when $\varepsilon = 1$ where the rewritten equation takes the form of Eq. (8)):

$$\ln\left(\frac{(1-f)^{(1-\varepsilon)} - 1}{\varepsilon - 1}\right) = n(\ln k + \ln t) \quad (7)$$

$$\ln(-\ln(1-f)) = n(\ln k + \ln t). \quad (8)$$

By plotting the left-hand side of Eqs. (7) and (8) vs. $\ln t$ for different values of ε the results will yield straight lines, assuming the model with corresponding impingement parameter describes the real situation. This cannot, of course, be the case for all values of ε, instead it is possible to find an optimum value from the goodness of the fits. In Fig. 5, a selected number of ε-values (0.1, 1, 1.5, 2 and 3) are shown after 1000 °C for $Ti_{0.36}Al_{0.64}N$. There is clearly a transition from a negative curvature at low ε-values to a positive curvature at high ε-values and a similar trend is seen for all samples. By comparing the quality of all the linear fits, e.g. with the residual plots and the R^2-value, it is possible to determine which ε-values best describe the real situation. For this case, ε-values between 0.8 and 1.5 represent the best fits depending on composition and temperature. However, all ε-values are included in the further analysis to illustrate the weak influence of ε on the extracted activation energies.

The remaining steps are performed in an identical way for all ε-values, but for easier visualization of the different steps only the data for $\varepsilon = 1$ is shown although they do not necessarily represent the best fit in Fig. 5. Fig. 6 shows a representation of the left-hand side in Eq. (8) vs. $\ln t$ for all samples. Since the transformation starts around 950 °C for $Ti_{0.36}Al_{0.64}N$ and around 1000 °C for $Ti_{0.55}Al_{0.45}N$, the transformation has already reached a certain fraction under isothermal conditions for the higher temperatures. For the highest temperatures the transformed fractions are 0.2–0.3, depending on the composition. Hence, the transformation values below 0.2–0.3 are omitted for all samples in order to maintain consistency between the samples in Fig. 6. Transformed fractions above 0.85–0.90 are also omitted as the noise for these values induces large fluctuations in Eq. (8) due to the logarithmic expression.

From Eqs. (7) and (8) it is easily seen that the intersection with the y-axis in Fig. 6 (and the remaining ε-values which are not shown) is identical to $n \cdot \ln k$ where n is the slope of the curve. $\ln k$ is needed in order to determine the activation energy, and this can be realized if Eq. (4) is rewritten as Eq. (9):

$$\ln k = \ln k_0 - \frac{E_a}{RT}. \quad (9)$$

Hence, a plot of $\ln k$ vs. $1/T$ will result in straight lines with a slope determined by the activation energy, E_a. This is shown in Fig. 7 for selected ε-values. The activation energy is to a large extent unaffected by the choice of ε and composition as the slopes are very similar. The appropriate fits are therefore chosen based on the goodness of the fitting procedure in Fig. 5, which was, as previously mentioned, best for ε-values between 0.8 and 1.5. It also suggests that the amount of impingement influencing the transformation is low.

The activation energy, as calculated from the slopes in Fig. 7, is shown as a function of ε-values between 0.8 and 1.5 in Fig. 8. An activation energy of 320 ± 10 kJ mol^{-1} is obtained for $Ti_{0.36}Al_{0.64}N$ and 350 ± 40 kJ mol^{-1} for $Ti_{0.55}Al_{0.45}N$ by considering the data for the different ε-values. These data are consistent with the experimentally obtained activation energy from Mayrhofer et al. [32] where the authors used the Kissinger equation [45] in combination with DSC data to calculate an activation energy
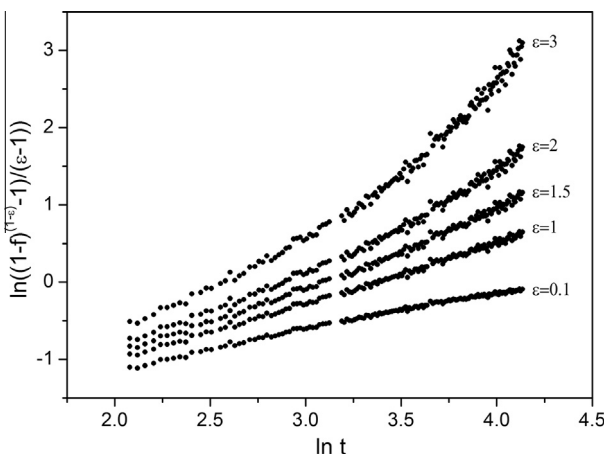

Fig. 5. Plots of the data after calculations according to Eq. (7) (and Eq. (8) for $\varepsilon = 1$) for a selected number of ε-values.
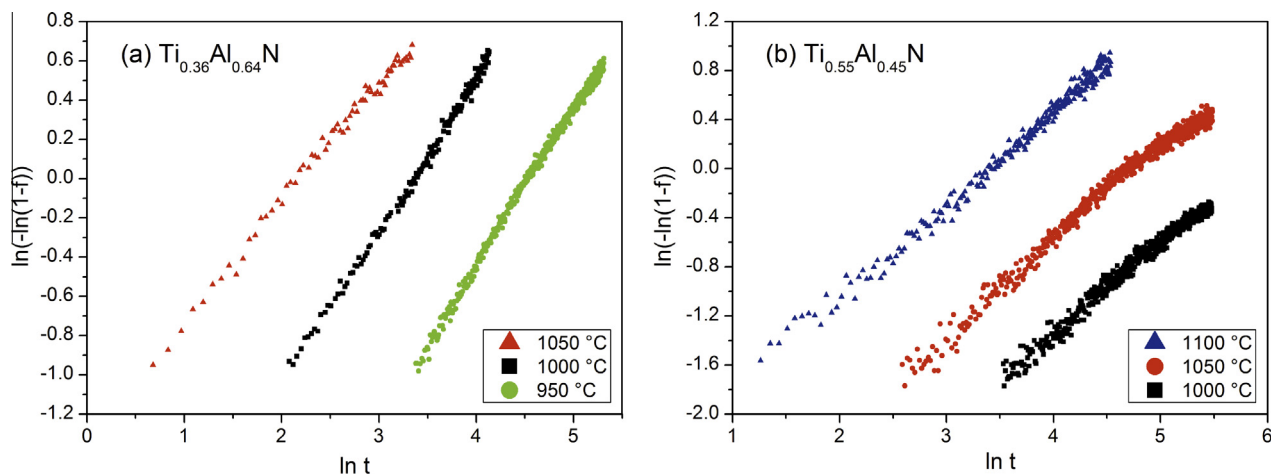
Fig. 6. KJMA plots at the different isothermal temperatures for (a) $Ti_{0.36}Al_{0.64}N$ and (b) $Ti_{0.36}Al_{0.64}N$. By fitting the data, the slopes and intersection with the y-axis can be extracted.
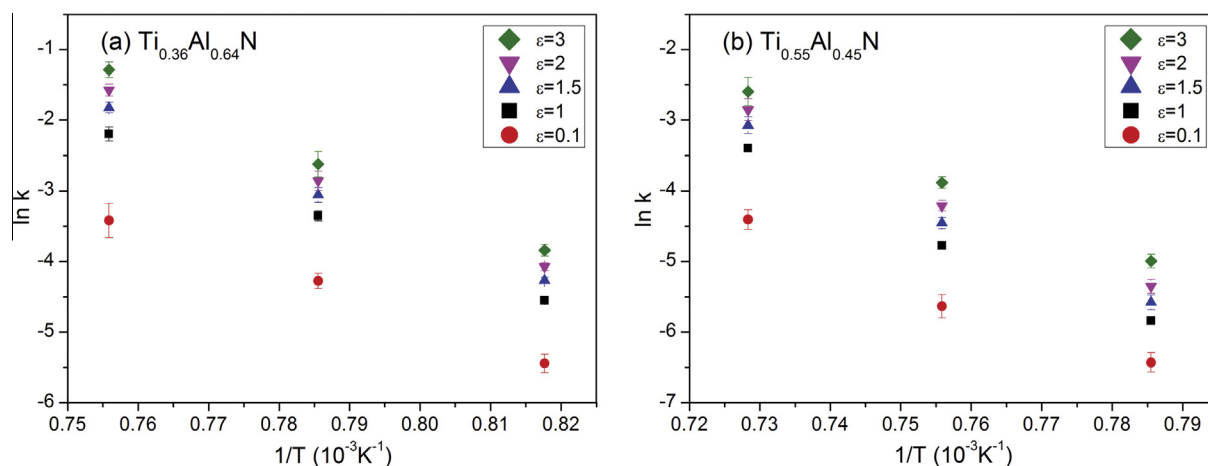

Fig. 7. Values for ln k vs. the reciprocal temperature for both compositions; the fitting of the linear slopes is used to calculate the activation energy of the transformation.
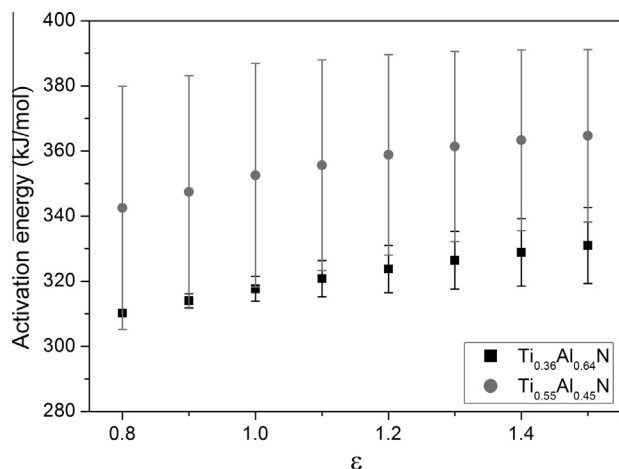

Fig. 8. Activation energies calculated as a function of ε-values. The larger error bars for $Ti_{0.55}Al_{0.45}N$ are due to the noisier data acquired during measurement.

of 350 kJ mol^{-1} for $Ti_{0.36}Al_{0.64}N$. Considering the large difference in transformation rate between the two compositions, the similarity in activation energies is notable. However, this result is expected as the activation energy is related to the transformation from a c-AlN domain into h-AlN. Although one could envision a situation where c-TiAlN transforms directly to c-TiN and h-AlN without a proceeding spinodal decomposition, e.g. in column/grain boundaries it is well documented that this is not the case away from the boundaries. Instead the process invokes a nearly complete chemical segregation of AlN and TiN while remaining in the face-centered cubic crystal structure (spinodal decomposition) prior to the transformation to h-AlN. Note that the spinodal decomposition is completed when TiN and AlN are separated. According to a previous study [17] the spinodal decomposition occurs in the first minutes (<5 min) during isothermal annealing at 850 and 900 °C. After the completion of the spinodal decomposition a coarsening stage begins where the domains grow to minimize the gradient energy and it occurs over a much

larger time span (180 min). Hence, the transformation to h-AlN occurs after the spinodal decomposition but concurrently with the coarsening of the cubic domains. The coarsening is also the reason why one observes an overlap between the peaks from spinodal decomposition + coarsening and h-AlN formation in DSC [32,46]. The only case when one could have spinodal decomposition occurring at the same time hexagonal transformation is in the vacancy-depleted regions next to grain boundaries. However, this contribution is extremely small in the presented data.

The validity of KJMA kinetics in a dual-phase structure is also discussed by Huang et al. [47], who obtained activation energies for ferrite recrystallization in two different steels (Fe–C–Mn–Mo and Fe–C–Mn–Si). Despite the dual-phase microstructure and two different compositions, the activation energies were identical but with large differences in recrystallization rates, i.e. very similar to what is seen in $Ti_{1-x}Al_xN$. Thus, the reason for the difference in transformation rate has a different origin and a likely explanation is the morphology of the microstructure prior to transformation, which is discussed in the next section.

3.3. Microstructural analysis

Fig. 9 shows a STEM micrograph with bright TiN-rich and dark AlN-rich domains after annealing $Ti_{0.55}Al_{0.45}N$ for 4 h at 1100 °C (Fig. 9a) and a HRTEM micrograph (Fig. 9b) obtained from the area marked with the square in Fig. 9a; Fig. 9c shows the SAED pattern of from the entire powder particle seen in Fig. 9a. The HRTEM micrograph, with the incident electron beam parallel with the [0 0 1] direction of c-TiN, reveals a h-AlN domain incoherently surrounded by c-TiN. There are some fringes from c-TiN seen in the h-AlN domain, which are due to domain overlap projection. The c-TiN/h-AlN interface is clearly parallel to the (2 2 0) lattice plane of c-TiN. The SAED pattern shows the {2 0 0} lattice plane reflections from c-TiN in combination with reflections from h-100 which are not as

strongly oriented as the c-TiN reflections, indicating a more random microstructure. Fig. 10a shows a STEM micrograph after annealing $Ti_{0.36}Al_{0.64}N$ for 4 h at 950 °C, and Fig. 10b shows the corresponding SAED pattern. The reflections from h-AlN in $Ti_{0.36}Al_{0.64}N$ reveal a similar morphology as the h-AlN reflections in $Ti_{0.55}Al_{0.45}N$ (Fig. 9c).

The samples in Figs. 9 and 10 are both in a late stage of the transformation (cf. Fig. 4) even though there is a large difference in annealing temperature. There is a notable difference in the microstructure: the domains in $Ti_{0.55}Al_{0.45}N$ are isolated, whereas the domains in $Ti_{0.36}Al_{0.64}N$ seem to be interconnected. The TEM samples are thick in comparison to the domains and projection artifacts may affect the interpretation. However, the c-TiN/h-AlN microstructures show a striking resemblance with the reported microstructures after spinodal decomposition into c-TiN/c-AlN for the same compositions [30,46], i.e. the only difference being the transformation of c-AlN to h-AlN. This means that the microstructure of the completely transformed material has inherited its microstructure from the one that evolved during spinodal decomposition and the subsequent coarsening when AlN still was in a cubic state. The microstructure evolution during spinodal decomposition is influenced by the elastic anisotropy of the alloy and for the two alloys discussed here $Ti_{0.36}Al_{0.64}N$ is more anisotropic than $Ti_{0.55}Al_{0.45}N$ [15]. A higher elastic anisotropy results in more elongated domains in the more compliant directions, i.e. along $\langle 200 \rangle$ [17,30]. The more elongated domains together with the higher volume fraction of AlN in $Ti_{0.36}Al_{0.64}N$ makes an interconnected coral-like structure of the h-AlN likely and consistent with the TEM observations. The differences in the microstructure between the two alloys would also explain the large difference in
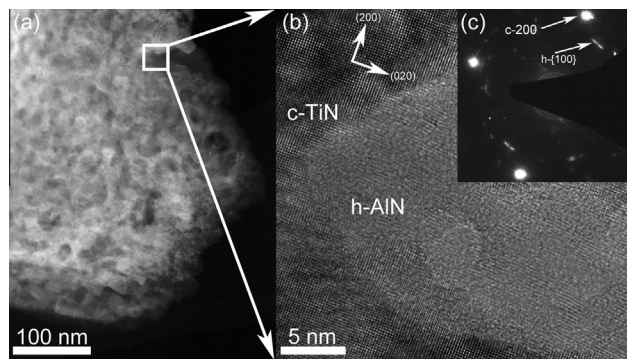

Fig. 9. (a) STEM micrograph showing a $Ti_{0.55}Al_{0.45}N$ powder particle after 4 h at 1100 °C with (b) a HRTEM micrograph showing an incoherent h-AlN area surrounded by c-TiN taken from the area inside the square with the incident electron beam parallel to the [0 0 1] direction of c-TiN and (c) a SAED pattern obtained from the entire powder particle. The arrows in the HRTEM micrograph denote the directions in c-TiN.
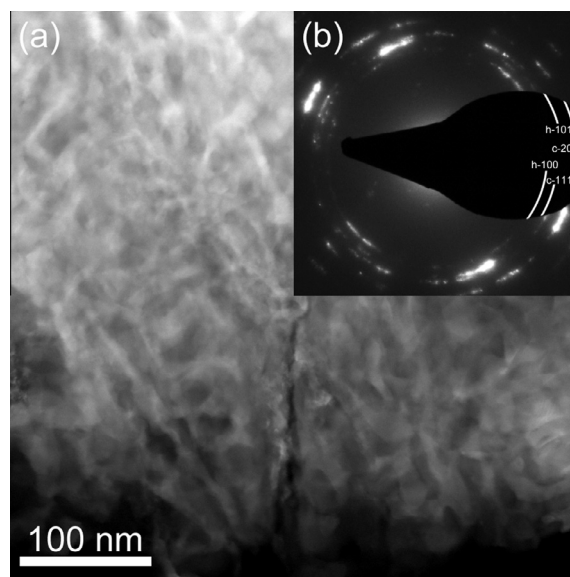

Fig. 10. (a) STEM micrograph showing a $Ti_{0.36}Al_{0.64}N$ powder particle after 4 h at 950 °C with (b) a SAED pattern obtained from the entire powder particle.

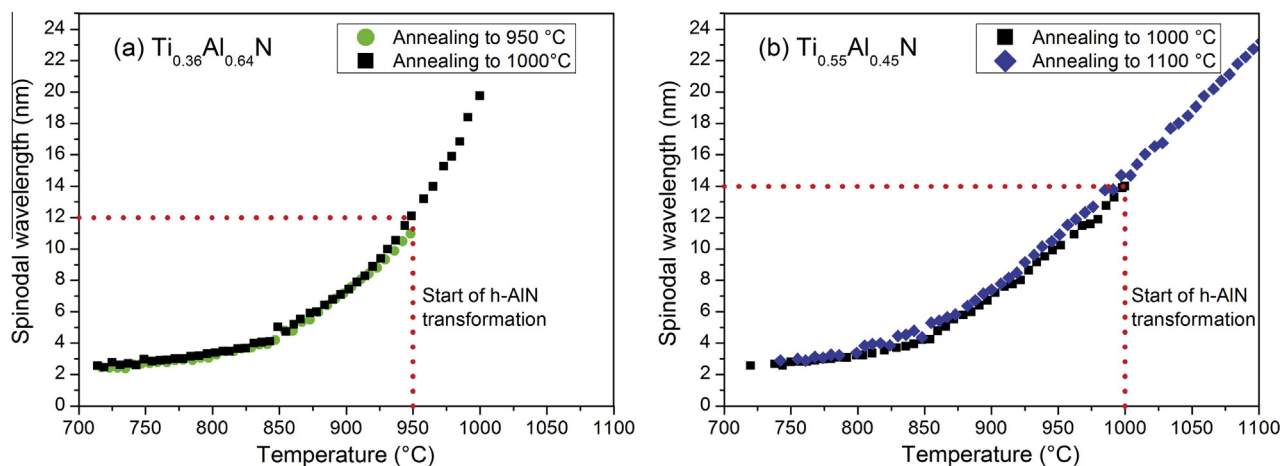Fig. 11. Evolution of the spinodal wavelength with increasing time for (a) $Ti_{0.36}Al_{0.64}N$ and (b) $Ti_{0.55}Al_{0.45}N$.

transformation rate despite their similar activation energies. The more frequent occurrence of interconnected c-AlN-rich domains in the high-Al-content alloy results in a faster transformation since fewer nuclei are needed to initiate transformation over a larger distance, i.e. the transformation is less affected by TiN–AlN interfaces. It has also been shown previously that TiN stabilizes c-AlN [27–29], which means that the larger amount of c-TiN surrounding the c-AlN in $Ti_{0.55}Al_{0.45}N$ suppresses the hexagonal transformation.

The critical wavelength of the cubic domains for the initiation of the transformation to h-AlN can be extracted from the SAXS measurements shown in Fig. 11 where the results after four individual runs are shown. From the SAXS analysis, a radius of gyration, R_G, is obtained which is related to the spinodal wavelength by assuming spherical c-TiN/AlN domains and multiplying the radius ($R = 1.29R_G$) [48] by 4. Although the assumption of spherical c-TiN/AlN domains is incorrect due to the anisotropic microstructure, it has been used in previous works [16,17] and comparisons with TEM indicate that only a minor

error results from this simplification. Fig. 11 shows initiation of spinodal decomposition at temperatures around 700 °C with an initial wavelength of 2–3 nm. The start of h-AlN transformation is determined to be around 950 °C for $Ti_{0.36}Al_{0.64}N$ and around 1000 °C for $Ti_{0.55}Al_{0.45}N$. This temperature was determined with support from WAXS data, i.e. when the $(1\,0\,0)$-peak was visible. Based on the three temperatures used, the precision is better than $\pm10°$. As seen in Fig. 11, the corresponding critical wavelengths are 12 and 14 nm, and although the difference is relatively small, it further supports the stabilization of c-AlN by the larger amount of c-TiN in $Ti_{0.55}Al_{0.45}N$. Also noteworthy is the indication of a small relative temperature difference between the samples, demonstrated by the identical evolution of the spinodal wavelength with the four individual measurements.

Fig. 12 shows the variation in *d*-spacings determined from the center of the h-100 diffraction line for all temperatures and compositions as a function of time from the start of the transformation. Except for the very first data points, the *d*-spacings seem to reach a minimum in the
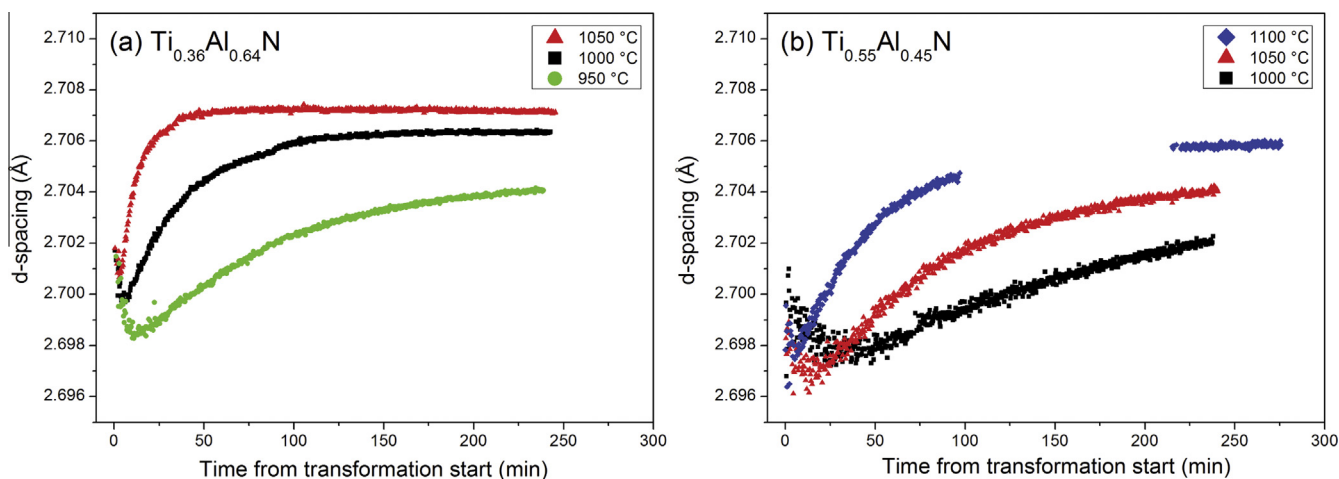

Fig. 12. Variation of the h-100 *d*-spacing with respect to transformation time for (a) $Ti_{0.36}Al_{0.64}N$ and (b) $Ti_{0.55}Al_{0.45}N$.
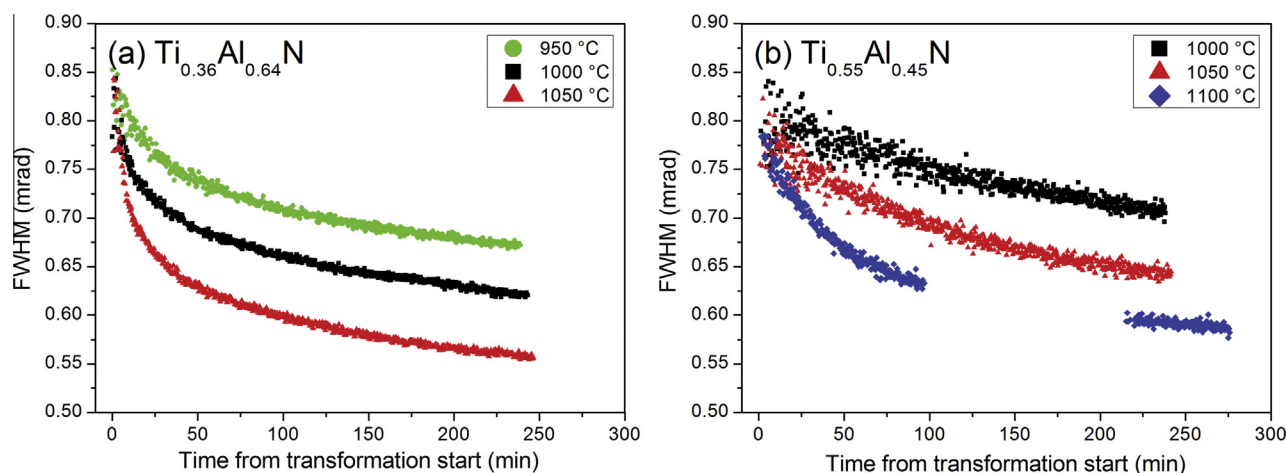
Fig. 13. FWHM of the h-100 peak in mrad with respect to transformation time for (a) $Ti_{0.36}Al_{0.64}N$ and (b) $Ti_{0.55}Al_{0.45}N$.

beginning of the transformation before they gradually increase towards or to a saturated value determined by the temperature. As the isothermal conditions are reached within the first 10 min after the transformation start, the subsequent increase in *d*-spacing cannot be explained solely by thermal expansion. These results can instead be explained either by the appearance of strained crystallites of h-AlN in the early transformation stage as discussed by Rogström et al. [46], or by the volume expansion associated with the cubic to hexagonal transformation. Another explanation is an early stage coherence between c-TiN/h-AlN as discussed for c-ZrN/h-AlN by Ghafoor et al. [49]. A combination of the mechanisms might also be valid in this case.

The FWHM values including instrumental broadening (0.15 mrad) of the h-100 peak are seen in Fig. 13 for $Ti_{0.36}Al_{0.64}N$ and $Ti_{0.55}Al_{0.45}N$. Peak broadening is mainly attributed to microstrain and is inversely related to domain size so the decrease in FWHM with time and temperature is related to an increased domain size and decreased microstrain. This is further supported by the identical FWHM values in the beginning of the transformation for both compositions. If the domain size is inversely proportional to the FWHM, as implied by the Scherrer equation, it can be seen from Fig. 13 that the relative domain sizes between the start and end of the transformation is not large, thus indicating a slow growth of the domains. This is further supported by the relatively small domains of h-AlN seen in the STEM micrographs in Figs. 9 and 10.

4. Conclusions

In this work the transformation from c-AlN to h-AlN under isothermal conditions for $Ti_{0.55}Al_{0.45}N$ and $Ti_{0.36}Al_{0.64}N$ has been studied by in situ high-energy synchrotron X-ray scattering. A strong correlation with Al content is found, and the transformation rate is higher in the high-Al-content alloy. The diffusion-limited transformation is also strongly temperature dependent.

KJMA analysis describes the kinetics of the transformation very well and yields activation energies of 320 ± 10 kJ mol^{-1} for $Ti_{0.36}Al_{0.64}N$ and 350 ± 40 kJ mol^{-1} for $Ti_{0.55}Al_{0.45}N$. The effect of grain boundaries on the transformation kinetics is negligible; rather, it is the degree of interconnection between the c-AlN domains that affects the transformation rate. The evolution of the spinodal wavelength with time shows a critical wavelength, for nucleation of h-AlN, of 12 nm for $Ti_{0.36}Al_{0.64}N$ and 14 nm for $Ti_{0.55}Al_{0.45}N$. The resulting microstructure of c-TiN/h-AlN is inherited from the preceding spinodal decomposition and only slow h-AlN domain growth is observed.

References

[1] Knotek O, Bohmer M, Leyendecker T. J Vac Technol A 1986;4:2695.
[2] Jehn HA, Hofmann S, Ruckborn VE, Munz WD. J Vac Technol A 1986;4:2701.
[3] Mayrhofer PH, Music D, Schneider JM. Appl Phys Lett 2006;88.
[4] Mayrhofer PH, Fischer FD, Böhm HJ, Mitterer C, Schneider JM. Acta Mater 2007;55:1441.
[5] Alling B, Ruban AV, Karimi A, Hultman L, Abrikosov IA. Phys Rev B 2011;83:104203.
[6] Alling B, Steneteg P, Tholander C, Tasnádi F, Petrov I, Greene JE, et al. Phys Rev B 2012;85:245422.
[7] Alling B, Ruban AV, Karimi A, Peil OE, Simak SI, Hultman L, et al. Phys Rev B 2007;75:045123.
[8] Johnson LJS, Thuvander M, Stiller K, Odén M, Hultman L. Thin Solid Films 2012;520:4362.
[9] Rachbauer R, Massl S, Stergar E, Holec D, Kiener D, Keckes J, et al. J Appl Phys 2011;110:023515.

[10] Rachbauer R, Stergar E, Massl S, Moser M, Mayrhofer PH. Scr Mater 2009;61:725.

[11] Hörling A, Hultman L, Odén M, Sjölén J, Karlsson L. J Vac Technol A 2002;20:1815.

[12] Hörling A, Hultman L, Odén M, Sjölén J, Karlsson L. Surf Coat Technol 2005;191:384.

[13] Norrby N, Johansson MP, M'Saoubi R, Odén M. Surf Coat Technol 2012;209:203.

[14] Bouzakis KD, Skordaris G, Gerardis S, Katirtzoglou G, Makrimallakis S, Pappa M, et al. Surf Coat Technol 2009;204:1061.

[15] Tasnádi F, Abrikosov IA, Rogström L, Almer J, Johansson MP, Odén M. Appl Phys Lett 2010;97:231902.

[16] Odén M, Rogström L, Knutsson A, Terner MR, Hedström P, Almer J, et al. Appl Phys Lett 2009;94:053114.

[17] Knutsson A, Ullbrand J, Rogström L, Norrby N, Johnson LJS, Hultman L, et al. J Appl Phys 2013;113:213518.

[18] Rafaja D, Wüstefeld C, Baehtz C, Klemm V, Dopita M, Motylenko M, et al. Metall Mater Trans A 2011;42:559.

[19] Rafaja D, Poklad A, Klemm V, Schreiber G, Heger D, Šíma M, et al. Thin Solid Films 2006;514:240.

[20] Forsén R, Johansson M, Odén M, Ghafoor N. J Vac Technol A 2012;30:061506.

[21] Lind H, Forsén R, Alling B, Ghafoor N, Tasndi F, Johansson MP, et al. Appl Phys Lett 2011;99:091903.

[22] Holec D, Zhou L, Rachbauer R, Mayrhofer PH. J Appl Phys 2013;113:113510.

[23] Rachbauer R, Blutmager A, Holec D, Mayrhofer PH. Surf Coat Technol 2012;206:2667.

[24] Rachbauer R, Holec D, Mayrhofer PH. Surf Coat Technol 2012;211:98.

[25] Riedl H, Holec D, Rachbauer R, Polcik P, Hollerweger R, Paulitsch J, et al. Surf Coat Technol 2013;235:174.

[26] Alling B, Odén M, Hultman L, Abrikosov IA. Appl Phys Lett 2009;95:181906.

[27] Norrby N, Lind H, Parakhonskiy G, Johansson MP, Tasnádi F, Dubrovinsky LS, et al. J Appl Phys 2013;113:053515.

[28] Knutsson A, Johansson MP, Persson POÅ, Hultman L, Odén M. Appl Phys Lett 2008;93:143110.

[29] Knutsson A, Johansson MP, Karlsson L, Odén M. J Appl Phys 2010;108:044312.

[30] Johansson-Jöesaar MP, Norrby N, Ullbrand J, M'Saoubi R, Odén M. Surf Coat Technol 2013;235:181.

[31] Wüstefeld C, Rafaja D, Dopita M, Motylenko M, Baehtz C, Michotte C, et al. Surf Coat Technol 2011;206:1727.

[32] Mayrhofer PH, Hörling A, Karlsson L, Sjölén J, Larsson T, Mitterer C, et al. Appl Phys Lett 2003;83:2049.

[33] Hammersley AP. ESRF internal report. ESRF97HA02T; 1997.

[34] Ilavsky J, Jemian PR. J Appl Crystallogr 2009;42:347.

[35] Ganesh BJ, Raju S, Rai AK, Vijayalakshmi M. Trans Indian Inst Met 2011;64:93.

[36] Jimenez-Melero E, Blondé R, Sherif MY, Honkimäki V, Van Dijk NH. Acta Mater 2013;61:1154.

[37] Khatibi A, Lu J, Jensen J, Eklund P, Hultman L. Surf Coat Technol 2012;206:3216.

[38] Avrami M. J Chem Phys 1939;7:1103.

[39] Avrami M. J Chem Phys 1940;8:212.

[40] Avrami M. J Chem Phys 1941;9:177.

[41] Johnson WA, Mehl RF. Trans AIME 1939;135:416.

[42] Forsén R, Johansson MP, Odén M, Ghafoor N. Thin Solid Films 2013;534:394.

[43] Jägle EA, Mittemeijer EJ. Acta Mater 2011;59:5775.

[44] Molnar D, Niedermeier C, Mora A, Binkele P, Schmauder S. Continuum Mech Thermodyn 2012;24:607.

[45] Kissinger HE. Anal Chem 1957;29:1702.

[46] Rogström L, Ullbrand J, Almer J, Hultman L, Jansson B, Odén M. Thin Solid Films 2012;520:5542.

[47] Huang J, Poole WJ, Militzer M. Metall Mater Trans A: Phys Metall Mater Sci 2004;35A:3363.

[48] Beaucage G. J Appl Crystallogr 1995;28:717.

[49] Ghafoor N, Johnson LJS, Klenov DO, Demeulemeester J, Desjardins P, Petrov I, et al. Appl Phys Lett Mater 2013;1:022105.